

Bleeding technique to control flow separation in hypersonic intakes

Sandesh Kunwar¹, Manjil Sitoula², Juluru Sandeep³

¹Dept of Mechanical and Aerospace engineering, Tribhuvan University, IOE Pulchowk Campus

²FOSSEE IIT-Bombay

³Dept of Aeronautical Engineering, Institute of Aeronautical Engineering

Abstract

Flow separation in hypersonic scramjet intakes due to shock wave-boundary layer interaction (SWBLI) degrades total pressure recovery, promotes intake unstart and affects combustion efficiency directly. This study numerically investigates boundary layer bleeding as a passive flow control method on a 2D double compression ramp inlet-isolator geometry at Mach 5, 6 and 7 using density based solver rhoCentralFoam in OpenFOAM 2212. Three bleed slots placed at the isolator entrance with widths (2.809 mm, 3.5 mm, and 4.2135 mm) were evaluated against a no-bleed baseline. At the design Mach 5, the 2.809mm bleed slot improved total pressure recovery by 25.3% and 3.5 mm bleed slot improved it by 25.1% with visible suppression and shifting of recirculation bubble downstream. At off-design Mach 6 and 7, bleed effectiveness decreases showing Mach specific character of passive fixed-geometry bleed.

Keywords: Hypersonic Intake, SWBLI, Total pressure recovery, Oblique shock waves

1 Introduction

1.1 Background

The recent advancement in hypersonic flights have increased the interest for single stage to orbit or double stage to orbit vehicles. To ensure SSTO or DSTO, supersonic combustion ramjets (Scramjet) engine are essential for hypersonic flights. Scramjet technology enables for high speed air-breathing vehicles which can be used for long-range strike vehicles, access-to-space missions and quick global transport. Unlike conventional turbine-based engines, scramjets consist of no rotating components, instead they rely on vehicles own forward motion to compress the incoming air for combustion, making them best suited for hypersonic flights in Mach 5-15 range (Idris et al., 2014).

Conceptually, the scramjet engine is an evolution of ramjet where the incoming supersonic airflow is slowed to subsonic speed before fuel injection and combustion. However when reaching to a speed of Mach 5, decelerating the air to subsonic speed would raise the stagnation temperature to very high which could cause molecular dissociation, ionization and extreme structural heat load making engine impractical. Thus for hypersonic speed $M > 5$, scramjet resolves the problem by allowing supersonic combustion which is the only thermodynamically viable option.

A scramjet engine is functionally divided into four components: the inlet (or intake), the isolator, the combustor and the nozzle. As illustrated in the generic engine schematic in Figure.1. The

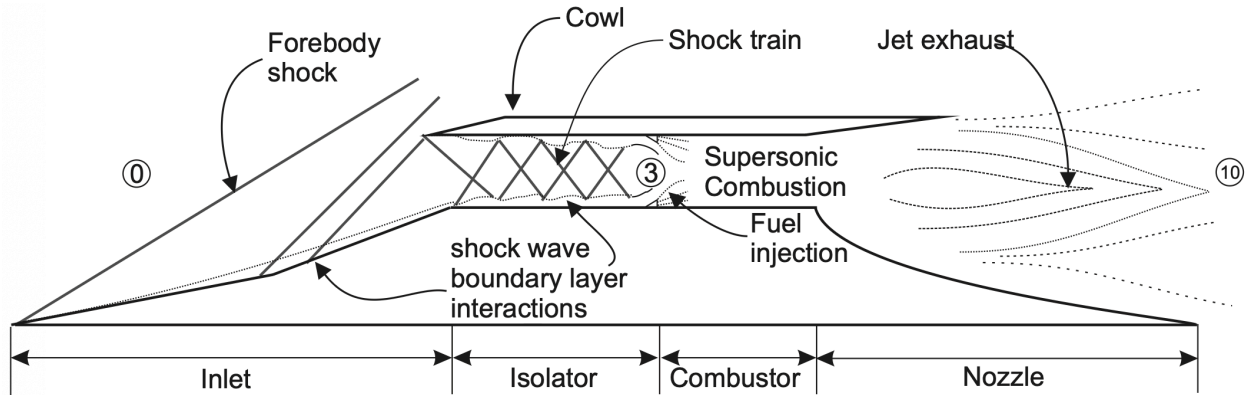


Figure 1: Schematics of a scramjet engine where the compression occurs between station 0 and 3 (Idris et al., 2014)

inlet is responsible for capturing the freestream hypersonic airflow and compressing it through a sequence of oblique shock waves generated by compression ramps and the cowl geometry. The isolator is a constant area or a mild diverging duct between the inlet throat and the combustor entrance containing the high pressure shock train. The combustor is the region where where fuel is injected and mixed with the supersonic air and burned in a very short amount of residence time. Finally, the nozzle expands the hot, high pressure gas to produce the necessary thrust.

The hypersonic intake, which is the focus of the present study compresses the incoming flow and

is considered as the most aerodynamically complex and performance limiting element of the entire propulsion system. It dictates the Mach number, total pressure, temperature and flow uniformity entering the combustor, thus having a direct effect on combustion efficiency and engine's operability across its intended flight envelope(Sandeep & Gupta, 2023).

1.2 Literature Review

Scramjet engines rely entirely on their inlet-isolator to compress hypersonic flow to conditions suitable for supersonic combustion. The inlet does this through a series of oblique shocks generated by compression ramps and the efficiency of this process is measured by total pressure recovery and kinetic energy efficiency which directly governs engine thrust. These shocks interact with the boundary layer and if the resulting adverse pressure gradient exceeds the momentum available in the near-wall fluid, flow separation occurs. Idris et al.(Idris et al., 2014) demonstrated experimentally using pressure-sensitive paint(PSP) on a generic Mach 5 two-dimensional scramjet inlet that three distinct separation bubbles form inside the isolator under nominal conditions, collectively reducing the effective entrance height by approximately 70% and depressing total pressure recovery to just 32%. This experimental baseline has been adopted as the validation reference for a series of computational investigations(Bajaj et al., 2025; Sandeep & Gupta, 2024; Sandeep & Gupta, 2023).

Sandeep and Gupta(Sandeep & Gupta, 2023) used this geometry to establish a reliable CFD framework for hypersonic intake simulation, comparing the Spalart-Allmaras, $k-\epsilon$ and SST $k-\omega$ turbulence models. Only SST $k-\omega$ reproduced all the key flow features simultaneously including the shoulder separation bubble, cowl-tip separation and downstream reattachment shocks. SA model failed to capture separation entirely and $k-\epsilon$ missed the cowl-tip interaction. Their grid-adaptive technique refining the mesh selectively in high pressure gradient regions achieved a y^+ below 1 with approximately 395,000 cells and correctly resolved the shock-on-lip condition. In a follow-on study(Sandeep & Gupta, 2024), they applied the same framework across a wide range of off-design conditions finding that separation bubble size grows from 51.4% to 70% of isolator height as Mach number increases from 4 to 8, while total pressure recovery falls from 15% at Mach 5 to 1% at Mach 8.

To control this separation, Bajaj et al.(Bajaj et al., 2025) investigated the effect of four different bleed gap sizes at Mach 5 and observed an inconsistent relationship between bleed size and intake performance. Among the configurations studied, a bleed gap of 2.809 mm produced the best results increasing the average total pressure recovery by 20.7% compared to the baseline case without bleeding. Smaller gaps were unable to provide sufficient pressure relief while larger gaps removed excessive mass flow and resulted in lower performance gains. The largest bleed gap considered improved total pressure recovery by only 14.5%. The same study also examined the influence of cowl deflection angle and found it to be even more effective than bleeding alone. A cowl deflection of 4° increased total pressure recovery by 32.3% by redirecting the airflow to promote boundary-layer reattachment and modify the shock structure. The combined application of the optimum bleed gap and cowl deflection angle yielded superior performance compared to either technique individually, indicating that the two approaches influence different mechanisms governing flow separation. As an alternative approach, Sandeep and Gupta(Sandeep & Gupta, 2024) studied micro-jet injection into the boundary layer at the separation point, finding that the diamond shaped orifices at a 45° in-

jection angle with nine injectors and a mass flow rate below 4% of the intake mass flow reduced the separation bubble from 4 mm to 0.95 mm which was a reduction of approximately 76%.

Several important gaps remain. Two-dimensional geometries were only considered and Idris et al (Idris et al., 2014) noted that three-dimensional effects become significant near the sidewalls and at high angles of attack. Bleed configurations have only been assessed under free-flow conditions, without the back pressure that a real combustor would impose. Adaptive bleed systems capable of varying the bleed rate across the flight Mach range have not been demonstrated. Turbulence modelling under real flight enthalpy conditions remains uncertain, and the injection strategy of Sandeep and Gupta (Sandeep & Gupta, 2024) has only been validated at Mach 5, with its behaviour at higher Mach numbers left as future work. Addressing these gaps will require tighter integration of experimental, computational, and active control approaches.

2 Problem Statement

Hypersonic vehicles powered by Scramjet engines operate at challenging freestream conditions, where the Mach number is above 5. The intake-isolator system of such vehicle must efficiently compress the incoming air through a series of oblique shocks while providing a stable and uniform flow to the combustor. These oblique shock waves imposes a sharp adverse pressure gradient on the boundary layer growing along compression ramps and isolator walls. The low-momentum fluid within the boundary layer cannot sustain the pressure rise and flow separates forming recirculation bubble that narrows the flow passage, changes the shock structure and may cause intake unstart. This phenomena becomes more worse at off design mach numbers where the shock system no longer aligns with the intake geometry as intended thus flow control being essential.

Passive boundary layer bleed is one of the most effective and simple method of solving this SWBLI problems. In this the low energy fluid at the walls of inlet-isolator are removed before it encounters a strong shock preventing the boundary layer from accumulating sufficient momentum to separate. This bleed configuration stabilizes the shock, suppresses recirculation, maintains mass capture and preserves total pressure recovery, which directly affect the thrust of an engine. The challenge is the bleed slot geometry, its position, length, shape which determines the effectiveness of the control. Thus investigation of bleed geometry is necessary to identify the best configuration.

The experimental investigation of these phenomena at hypersonic conditions is very costly and complex as hypersonic wind tunnel facilities, instrumentation, and repeatability is difficult to maintain. Computational fluid dynamics overcomes these barriers by providing the detailed flow information across any domain at any operating condition, full flexibility in changing parameters and repetition of test at fraction of experimental cost. However most existing numerical studies on scramjet intake flows are carried out by commercial solvers, which carry licensing cost and reduce reproducibility of the work. OpenFOAM as a fully open-source CFD platform offers a flexible and accessible alternative, but its ability to accurately predict hypersonic flow, shock wave-boundary layer interactions and bleed-modified flow fields has not been sufficiently established. The present study address this gap by gap by developing and validating an OpenFOAM-based simulation of a Scramjet intake-isolator and investigating the effect of passive boundary layer bleed slot dimensions

on pressure distribution and total pressure recovery at the exit of isolator.

3 Governing Equations and Models

3.1 Governing Equations

The flow within the hypersonic intake was modeled by solving the compressible Reynolds-Averaged Navier-Stokes (RANS) equations using the density-based solver rhoCentralFoam. The governing equations consist of conservation of mass, momentum, and energy.

The continuity equation is

$$\frac{\partial \rho}{\partial t} + \nabla \cdot (\rho \mathbf{U}) = 0 \quad (1)$$

The momentum equation is

$$\frac{\partial(\rho \mathbf{U})}{\partial t} + \nabla \cdot (\rho \mathbf{U} \mathbf{U}) = -\nabla p + \nabla \cdot \boldsymbol{\tau} \quad (2)$$

where the viscous stress tensor is

$$\boldsymbol{\tau} = \mu_{\text{eff}} \left[\nabla \mathbf{U} + (\nabla \mathbf{U})^\top - \frac{2}{3} (\nabla \cdot \mathbf{U}) \mathbf{I} \right] \quad (3)$$

The effective dynamic viscosity μ_{eff} combines the molecular and turbulent contributions as

$$\mu_{\text{eff}} = \mu + \mu_t \quad (4)$$

with μ evaluated from Sutherland's law and μ_t supplied by the SST k - ω model.

The total energy equation is

$$\frac{\partial(\rho E)}{\partial t} + \nabla \cdot (\rho \mathbf{U} H) = \nabla \cdot (\alpha_{\text{eff}} \nabla h) + \nabla \cdot (\boldsymbol{\tau} \cdot \mathbf{U}) \quad (5)$$

where the total energy E and total enthalpy H are respectively defined as

$$E = h - \frac{p}{\rho} + \frac{|\mathbf{U}|^2}{2} \quad (6)$$

$$H = E + \frac{p}{\rho} \quad (7)$$

The effective thermal diffusivity α_{eff} couples the turbulence model to the energy equation as

$$\alpha_{\text{eff}} = \frac{\mu}{Pr} + \frac{\mu_t}{Pr_t} \quad (8)$$

where $Pr = 0.72$ is the laminar Prandtl number for air and $Pr_t = 0.85$ is the turbulent Prandtl number.

The thermodynamic properties of air were evaluated using the ideal gas equation of state

$$p = \rho RT \quad (9)$$

where p is the static pressure, ρ is the density, R is the specific gas constant, and T is the static temperature.

Dynamic viscosity was modelled using the Sutherland correlation as implemented in rhoCentralFoam

$$\mu = \frac{A_s T^{3/2}}{T + T_s} \quad (10)$$

where $A_s = 1.458 \times 10^{-6} \text{ kg/m}\cdot\text{s}\cdot\text{K}^{1/2}$ and $T_s = 110.4 \text{ K}$ are the standard Sutherland coefficients for dry air. At the freestream temperature $T_\infty = 63.75 \text{ K}$ corresponding to the Mach 5 inlet condition, this yields

$$\mu_\infty = \frac{1.458 \times 10^{-6} \times 63.75^{3/2}}{63.75 + 110.4} = 4.26 \times 10^{-6} \text{ Pa}\cdot\text{s} \quad (11)$$

The freestream density is obtained from the ideal gas law as $\rho_\infty = p_\infty / RT_\infty = 1228.52 / (287.1 \times 63.75) = 0.0671 \text{ kg/m}^3$, giving the kinematic viscosity

$$\nu_\infty = \frac{\mu_\infty}{\rho_\infty} = \frac{4.26 \times 10^{-6}}{0.0671} = 6.34 \times 10^{-5} \text{ m}^2/\text{s} \quad (12)$$

This value is used as the reference kinematic viscosity for the turbulence inlet conditions. The thermodynamic model uses the `hePsiThermo` framework with the perfect gas equation of state and a constant specific heat $C_p = 1005 \text{ J/kg}\cdot\text{K}$, consistent with the calorically perfect gas assumption. This assumption is valid for air at the conditions investigated here since vibrational excitation and molecular dissociation remain negligible below approximately Mach 8. The molecular weight of air is taken as 28.9 g/mol , giving a specific gas constant $R = 287.1 \text{ J/kg}\cdot\text{K}$, and the Sutherland coefficients $A_s = 1.458 \times 10^{-6} \text{ kg/m}\cdot\text{s}\cdot\text{K}^{0.5}$ and $T_s = 110.4 \text{ K}$ are the standard values for dry air.

3.2 Turbulence Modeling

The SST k - ω turbulence model (Menter, 1994) was used. The transport equations are

$$\frac{\partial(\rho k)}{\partial t} + \nabla \cdot (\rho \mathbf{U} k) = P_k - \beta^* \rho \omega k + \nabla \cdot [(\mu + \sigma_k \mu_t) \nabla k] \quad (13)$$

$$\frac{\partial(\rho \omega)}{\partial t} + \nabla \cdot (\rho \mathbf{U} \omega) = \frac{\alpha \rho}{\mu_t} P_k - \beta \rho \omega^2 + \nabla \cdot [(\mu + \sigma_\omega \mu_t) \nabla \omega] + 2(1 - F_1) \frac{\rho \sigma_\omega 2}{\omega} \nabla k \cdot \nabla \omega \quad (14)$$

where $P_k = \mu_t (2S_{ij}S_{ij} - \frac{2}{3}(\nabla \cdot \mathbf{U})^2) - \frac{2}{3}\rho k \nabla \cdot \mathbf{U}$ is the turbulence production term and the eddy viscosity is

$$\mu_t = \frac{\rho a_1 k}{\max(a_1 \omega, SF_2)} \quad (15)$$

The inlet turbulent kinetic energy was estimated from a freestream turbulence intensity of $I = 0.5\%$:

$$k = \frac{3}{2}(U_\infty I)^2 = \frac{3}{2}(800.5 \times 0.005)^2 = 24.03 \text{ m}^2/\text{s}^2 \quad (16)$$

3.3 Numerical Scheme

The simulations were performed using the density-based solver rhoCentralFoam in OpenFOAM, which employs the Kurganov-Tadmor (KT) central-upwind scheme for evaluating numerical fluxes across cell faces. The numerical flux at a cell interface is

$$\mathbf{F}_{i+\frac{1}{2}} = \frac{\omega_{i+\frac{1}{2}}^+ \mathbf{F}_L + \omega_{i+\frac{1}{2}}^- \mathbf{F}_R}{\omega_{i+\frac{1}{2}}^+ + \omega_{i+\frac{1}{2}}^-} - \frac{\omega_{i+\frac{1}{2}}}{2}(\mathbf{U}_R - \mathbf{U}_L) \quad (17)$$

where the local propagation speed is

$$\omega_{i+\frac{1}{2}} = \max(|\mathbf{u}_L| + c_L, |\mathbf{u}_R| + c_R) \quad (18)$$

and the local speed of sound is

$$c = \sqrt{\gamma RT} \quad (19)$$

This formulation captures shocks without a Riemann solver, making it well-suited for high-speed compressible flows with strong shocks and shock-wave/boundary-layer interactions.

The left and right interface states \mathbf{U}_L , \mathbf{U}_R , ρ_L , ρ_R , and T_L , T_R required by the flux formula are reconstructed using the van Leer TVD (Total Variation Diminishing) limiter. TVD reconstruction suppresses spurious oscillations across shock discontinuities while retaining second-order spatial accuracy in smooth flow regions. Gradients are evaluated using a second-order Gauss linear scheme. For the turbulence transport equations, a limitedLinear bounded scheme is used in place of the central scheme to prevent unphysical negative values of k and ω in the vicinity of strong shocks.

Temporal integration uses the explicit first-order Euler scheme. The time step is not fixed but is adjusted adaptively at every iteration to satisfy the acoustic Courant condition

$$\text{Co} = \frac{(|\mathbf{U}| + c) \Delta t}{\Delta x} \leq \text{Co}_{\max} \quad (20)$$

with $\text{Co}_{\max} = 0.5$. The initial time step is $\Delta t_0 = 10^{-9}$ s and the maximum permitted step is $\Delta t_{\max} = 10^{-7}$ s. Restricting the Courant number to 0.5 rather than the theoretical stability limit of 1.0 provides a margin of safety against the additional numerical stiffness introduced by the SST turbulence equations, which operate on timescales shorter than those of the main flow variables at the near-wall cell sizes required for $y^+ \approx 1$.

3.4 Hypersonic Intake Flow Physics and Performance Parameters

The compression process in a hypersonic intake operates through a sequence of oblique shock waves generated by the double compression ramp geometry. The flow physics governing this compression are described as oblique shock relations, which are foundational to understand the pressure recovery and flow separation behavior investigated in this study.

3.4.1 Mach Number

It is defined as the ratio of flow speed to the local speed of sound.

$$M = \frac{|U|}{c}, c = \sqrt{\gamma RT} \quad (21)$$

Where $\gamma = 1.4$ for air and $R = 287$ J/kg.K. At the inlet conditions used in this study ($T = 63.75$ K, $M_\infty = 5$), the free stream velocity is $U_\infty = 800.5$ m/s.

3.4.2 Oblique shock relation : $\theta - \beta - M$ relation

For a compression ramp of deflection angle θ , the shock wave angle β relative to the incoming flow is governed by the relation:

$$\tan \theta = 2 \cot \beta \frac{M_1^2 \sin^2 \beta - 1}{M_1^2 (\gamma + \cos 2\beta) + 2} \quad (22)$$

This must be solved iteratively for β given M_1 and θ . For the present geometry with a 10° first ramp and 22° second ramp at $M = 5$, the weak shock solution (attached oblique shock) gives $\beta_1 \approx 20.0^\circ$ and $\beta_2 \approx 35.6^\circ$ respectively. These angles determine where the oblique shocks impinge on the cowl and isolator walls, defining the regions of high adverse pressure gradient where boundary layer separation and bleed slots are relevant.

3.4.3 Static Pressure Ratio

Static pressure ratio across an oblique shock, depends only on the normal component of the upstream Mach number $M_1 \sin \beta$:

$$\frac{p_2}{p_1} = \frac{2\gamma M_1^2 \sin^2 \beta - (\gamma - 1)}{\gamma + 1} \quad (23)$$

3.4.4 Density Ratio

The density also depends only on the upstream normal component of flow as:

$$\frac{\rho_2}{\rho_1} = \frac{(\gamma + 1) M_1^2 \sin^2 \beta}{(\gamma - 1) M_1^2 \sin^2 \beta + 2} \quad (24)$$

3.4.5 Downstream Mach Number

Downstream Mach number after the oblique shock wave is calculated as:

$$M_2^2 \sin^2(\beta - \theta) = \frac{(\gamma - 1) M_1^2 \sin^2 \beta + 2}{2\gamma M_1^2 \sin^2 \beta - (\gamma - 1)} \quad (25)$$

The normal-shock limit ($\beta = 90^\circ$) gives the maximum possible pressure rise and the worst total pressure loss. Oblique shocks are preferred precisely because they achieve compression at lower entropy generation.

3.4.6 Stagnation quantities

For isentropic flow, the total (stagnation) pressure and temperature are related to the local static values by:

$$\frac{p_0}{p} = \left(1 + \frac{\gamma - 1}{2} M^2\right)^{\frac{\gamma}{\gamma - 1}}, \quad \frac{T_0}{T} = 1 + \frac{\gamma - 1}{2} M^2 \quad (26)$$

At $M = 5$, $T_\infty = 63.75$ K gives $T_0 = 63.75 \times (1 + 0.2 \times 25) = 382.5$ K, and $p_\infty = 1228.52$ Pa gives $p_{0,\infty} = 1228.52 \times (1 + 0.2 \times 25)^{3.5} \approx 529.3$ kPa.

3.4.7 Total Pressure Recovery (π)

Total pressure recovery is the primary performance metric of the intake-isolator system and is defined as:

$$\pi = \frac{\overline{p_{0,\text{exit}}}}{p_{0,\infty}} \quad (27)$$

where the overbar denotes the mass-flow-weighted average across the isolator exit plane. Every oblique shock and every separation bubble reduces π below unity. For reference, the inviscid isentropic case would give $\pi = 1$ by definition.

4 Computational domain

4.1 Reference Geometry

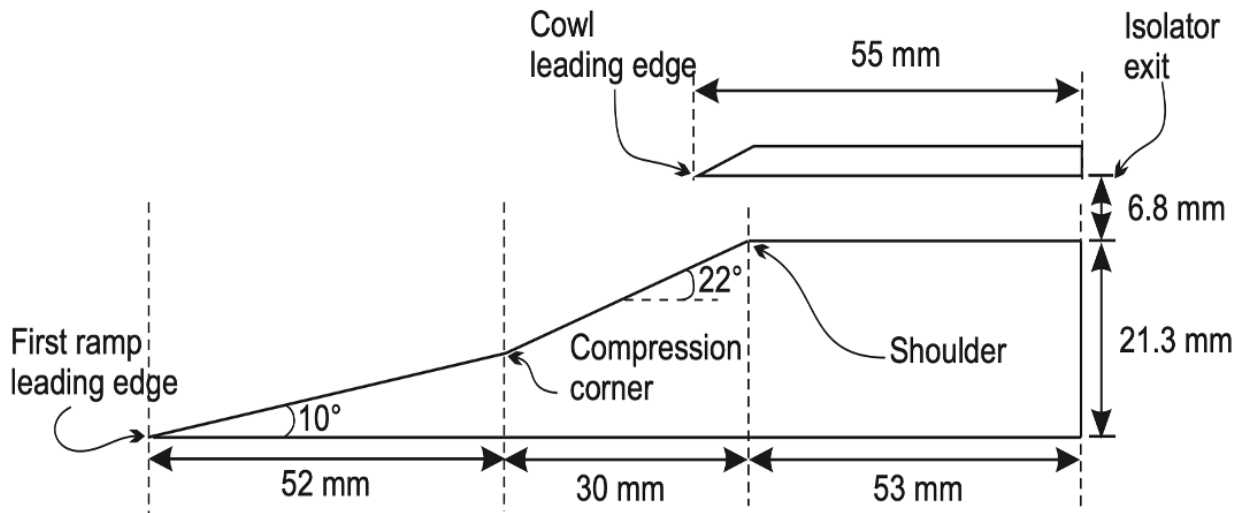


Figure 2: Basic scramjet inlet-isolator (Idris et al., 2014)

A specifically designed two dimensional double ramp inlet-isolator with a 3 shock inlet system was used as a reference geometry for the base case. The base case is the general inlet-isolator without any bleeding implemented. This geometry achieves a shock-on-lip (SoL) condition in Mach 5 flow, however the shock-on-lip isn't fulfilled for higher Mach flow which could be seen for Mach

6 and 7 cases. The ideal condition of shock-on-shoulder (SoS) was neglected and the cowl shock was deliberately designed to impinge downstream of the shoulder to satisfy the Kantrowitz limit (Kantrowitz & Donaldson, 1945). The resulting design is as shown in Fig:2 having a total length of 155 mm with an isolator height of 6.8mm and width of inlet as 36 mm (Idris et al., 2014).

The bleed geometry is similar to that of baseline geometry, a difference being bleed slots introduced at the isolator start. The length $L1$ in the Fig:3 is the bleed slot length, the three different lengths ($L1 = 2.809\text{mm}$, 3.5mm , 4.2135mm) are taken to evaluate the effect of the bleed slot on the the performance. $L3(12.9\text{mm})$ corresponds to the bleed opening at the base, $L2(29.09\text{mm})$ is the capture height and $L4(6.8\text{mm})$ is the outlet where compressed air exits the inlet and enters the combustor (Bajaj et al., 2025).

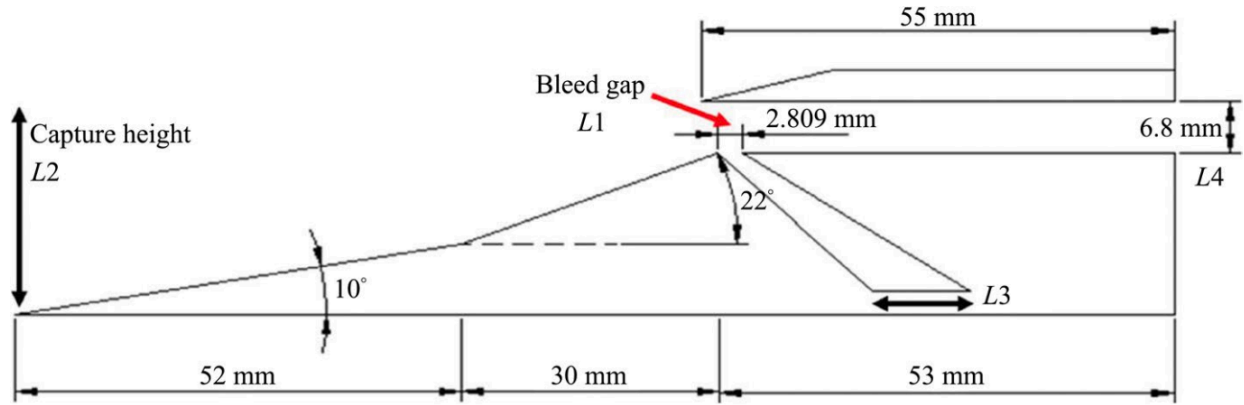


Figure 3: Bleed $L1$ incorporated in three different cases with length $L1$ varying as $L1 = 2.809\text{mm}$, 3.5 mm and 4.2135mm (Bajaj et al., 2025)

4.2 Computational Domain

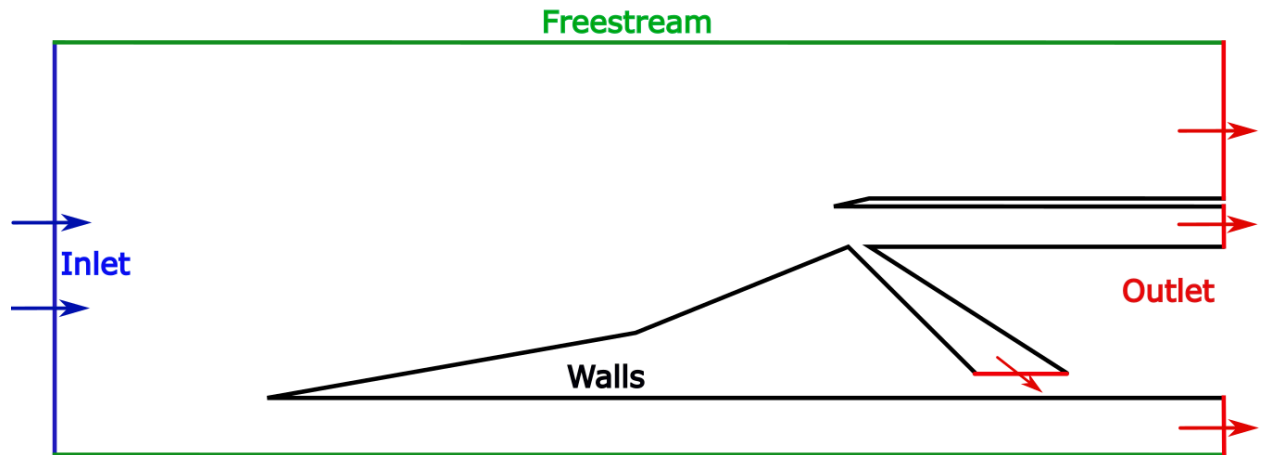


Figure 4: Bleed geometry computational domain

The computational domain was made according to reference geometries in Fig:2, 3. Fig:4 shows the domain with bleeding slot, for the base case the bleed slot is absent. This a 2-d computational domain, it consist of one inlet from where the flow comes in, the flow then encounters solid walls and then exits through 3 outlets (4 in case of bleed). The freestream ensures flow doesn't reflect of the external boundaries and uniform freestream condition is maintained. In case of bleed geometries the flow is also exited through the bleed slot thus acting as an outlet.

4.3 Meshing

The computational domain was discretized using OpenFOAM's blockMesh utility generating a fully structured, multi-block hexahedral mesh. The whole domain was divided into 12 hexahedral blocks, with a unit depth of 1 mm in the spanwise direction for 2-D flow. The total mesh count amounts to 1,46,820 cells across all blocks. Mesh density is highest in the regions of strong

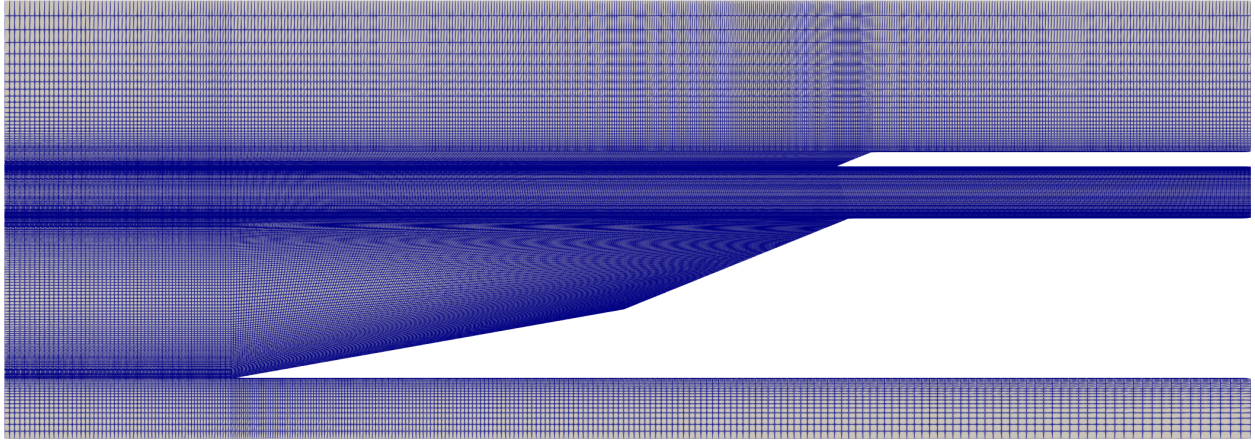


Figure 5: Mesh with 1,46,820 cells generated from blockMesh

flow conditions near the isolator and cowl which is done using simpleGrading. For maintaining $y^+ \approx 1$ wall grading was employed and the first cell height was set to $2\mu m$ as also mentioned in (Idris et al., 2014). The block near isolator were set with a multi-level bilinear grading of the form $((0.5 \ 0.5 \ 96.2) (0.5 \ 0.5 \ 0.01040))$ for maintaining the first cell height. The stream-wise grading ranges from 0.5 to 5 across the blocks, with finer cells toward the inlet to resolve the developing boundary layer on the fore-body and coarser cells toward the outlet. The upper domain blocks transitioning toward the far-field boundary use wall-normal gradings of 8 and 20 to avoid abrupt cell-size jumps. The front and back faces are assigned the empty boundary condition, which is the standard OpenFOAM treatment for two-dimensional cases. The checkMesh utility reported no errors, with a maximum face skewness of 2.3, confirming the mesh quality is within acceptable limits for the solver.

The bleed mesh is similar in all others aspects, the main changes are done in the isolator section. The isolator instead of one single block, it is split into three blocks for incorporating bleed. Thus the total blocks increase to 14 hexahedral blocks with total cells count of 1,49,920 cells as seen in Fig: 6.

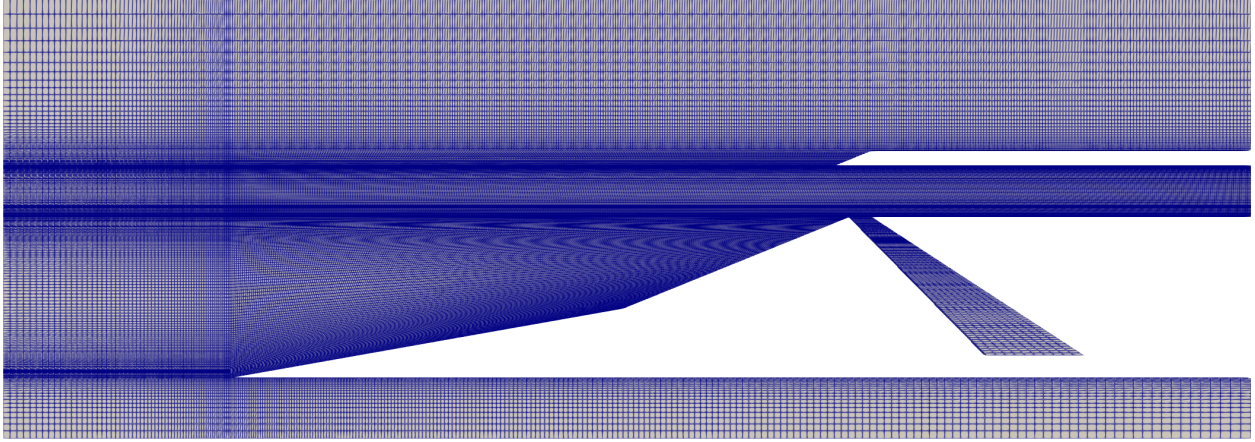


Figure 6: 2.809mm bleed slot mesh with 149,920 cells generated from blockMesh

4.4 Initial and Boundary Conditions

The simulation was performed for Mach 5 as the design condition with Mach 6 and Mach 7 as off-design conditions at the same altitude. Since altitude is held constant across all cases, the static temperature, pressure and density remain unchanged; only the velocity and the derived turbulent quantities scale with Mach number. All values reported are static quantities.

p - Pressure

- A fixed static pressure of 1228.52 Pa was applied at the inlet using `fixedValue`. The outlet and walls were assigned `zeroGradient` allowing pressure to adjust naturally through the equation of state.
- The freestream patch used `inletOutlet` with the same reference value to prevent non-physical backflow at the far-field boundary.

T - Temperature

- The freestream static temperature of 63.75 K, corresponding to high-altitude flight conditions, was prescribed at the inlet as `fixedValue`; the outlet used `zeroGradient`.
- The walls were assigned a `fixedValue` of 300 K representing an isothermal cold-wall condition.

U - Velocity

- A uniform freestream velocity $\mathbf{U}_\infty = (U_\infty, 0, 0) \text{ m s}^{-1}$ was applied at the inlet as `fixedValue`; the outlet and freestream used `inletOutlet` to allow smooth flow exit while preventing reverse inflow.
- The walls used the `noSlip` condition enforcing $\mathbf{U} = \mathbf{0}$, and the frontAndBack planes were set to empty consistent with the 2-D planar assumption.

k - Turbulent Kinetic Energy

- The inlet value was calculated from a freestream turbulence intensity of $I = 0.5\%$ using Eq.(??) and prescribed as `fixedValue`. At Mach 5 this gives $k = 24.03 \text{ m}^2 \text{ s}^{-2}$, scaling upward with velocity for higher Mach cases.
- At the walls, `kLowReWallFunction` was applied, consistent with the low-Reynolds-number near-wall treatment of the SST $k-\omega$ model; the outlet and freestream used `inletOutlet`.

ω - Specific Dissipation Rate

- The inlet value was computed using

$$\omega = \frac{k^{1/2}}{C_\mu^{1/4} L} \quad (28)$$

where $C_\mu = 0.09$ is the standard SST model constant and $L = 0.952 \text{ mm}$ is the turbulent length scale estimated from the inlet geometry. A `fixedValue` condition was applied.

- The walls used `omegaWallFunction` to apply the correct near-wall asymptotic behaviour; the outlet and freestream used `inletOutlet`.

ν_t - Turbulent Kinematic Viscosity

- Derived from the inlet turbulence quantities as $\nu_t = k/\omega$ and set to calculated at all non-wall patches, so the solver evaluates it from the local k and ω fields at each iteration.
- The walls used `nutUSpaldingWallFunction` which applies Spalding's blended wall law and remains valid across both the viscous sublayer and the log-law region, making it robust for the varying y^+ values encountered along the ramp and isolator walls.

α_t - Turbulent Thermal Diffusivity

- Initialised throughout the domain using

$$\alpha_t = \frac{\rho \nu_t}{Pr_t} \quad (29)$$

with a turbulent Prandtl number $Pr_t = 0.9$; it is set to calculated at all non-wall patches.

- The walls used `compressible::alphatWallFunction` to enforce the correct turbulent heat flux condition at the cold isothermal surface, which is important for accurate wall heat transfer prediction in hypersonic flow.

4.5 Solver Selection

The simulations were performed using `rhoCentralFoam` in OpenFOAM v2212, a density-based compressible solver built around the Kurganov-Tadmor (KT) central-upwind scheme for convective flux evaluation. Unlike pressure-based solvers such as `rhoPimpleFoam`, density-based formulations treat density as a primary variable and update pressure through the equation of state, making them better suited for flows dominated by strong shocks, large density gradients and hypersonic

Table 1: Inlet boundary condition values for all Mach cases. T , p , and ρ are constant across cases (same altitude). Turbulent quantities use $I = 0.5\%$, $L = 0.952$ mm, $Pr_t = 0.9$.

M	T_∞ (K)	p_∞ (Pa)	U_∞ (m s ⁻¹)	k (m ² s ⁻²)	ω (s ⁻¹)	ν_t (m ² s ⁻¹)	α_t (kg m ⁻¹ s ⁻¹)
5	63.75	1228.52	800.5	24.03	9402	2.557×10^{-3}	1.907×10^{-4}
6	63.75	1228.52	960.6	34.6	11280	3.067×10^{-3}	2.288×10^{-4}
7	63.75	1228.52	1120.7	47.09	13160	3.578×10^{-3}	2.669×10^{-4}

Mach numbers. Turbulence closure was provided by the SST k - ω model, which was selected on the basis of the comparative study by (Sandeep & Gupta, 2023), who demonstrated on the same reference geometry that SST k - ω is the only two-equation model that simultaneously reproduces the shoulder separation bubble, cowl-tip separation and downstream reattachment shocks, while the Spalart-Allmaras and k - ϵ models failed to capture these features.

5 Implementation in OpenFOAM

5.1 Case Setup Structure

The case was set up following the standard OpenFOAM three directory structure. The 0/ directory contains the initial and boundary condition files for all nine transported fields: U, p, T, rho, e, k, omega, nut, and alphasat. The energy field is stored as specific internal energy e rather than enthalpy h because the hePsiThermo framework was configured with sensibleInternalEnergy; density rho also appears as an explicit field since rhoCentralFoam treats it as a primary transported variable. The constant/ directory contains the polyMesh folder with the mesh generated by blockMesh, thermophysicalProperties defining the perfectGas equation of state with Sutherland viscosity and constant $C_p = 1005$ J kg⁻¹ K⁻¹, and turbulenceProperties specifying the RAS SST k - ω model. The system/ directory holds blockMeshDict, controlDict, fvSchemes, fvSolution, decomposeParDict, and setFieldsDict(only for bleed cases).

5.2 Control Dictionary

The key runtime parameters set in controlDict are listed in Table 2. The simulation was run with adaptive time-stepping governed by the acoustic Courant condition with $Co_{\max} = 0.5$, which provides a margin of safety against the additional numerical stiffness introduced by the near-wall SST model cells at the $y^+ \approx 1$ resolution. The initial time step of $\Delta t_0 = 10^{-9}$ s is necessary to avoid divergence at startup when the flow field is still uniform and the solver has not yet established the shock structure. Two runtime function objects were active throughout: MachNo to compute and write the Mach number field at every write interval, and fieldMinMax to monitor the global minimum and maximum of rho, p, T, and U at each time step as a convergence and stability check.

Table 2: Key controlDict parameters used in all simulations.

Parameter	Value	Description
application	rhoCentralFoam	Density-based compressible solver
endTime	1.5×10^{-3} s	Total physical simulation time
deltaT	1×10^{-9} s	Initial time step
adjustTimeStep	yes	Adaptive time-stepping enabled
maxCo	0.5	Maximum acoustic Courant number
maxDeltaT	1×10^{-7} s	Maximum permitted time step
writeInterval	1×10^{-4} s	Solution written every 0.1 ms
writeFormat	ascii	Human-readable output format

5.3 Running Procedure

The geometry was meshed using `blockMesh` and the quality of the mesh was verified using `checkMesh`. All simulations were run in parallel across 4 processors. The domain was decomposed using `decomposePar` prior to launching the solver. The simulation was then executed using:

```
blockMesh
checkMesh
setFields      \\For bleed cases only
decomposePar
mpirun -np 4 rhoCentralFoam -parallel > log.rhoCentralFoam 2>&1 &
reconstructPar
```

After completion, `reconstructPar` was used to reassemble the decomposed processor directories into a single time-series for post-processing.

For the bleed cases, an additional initialization step was required before the solver was launched. The `setFields` utility was used to override the uniform freestream initial condition inside the bleed slot region with a localized zero-velocity, near-zero turbulence state. This prevents the solver from starting with a non-physical supersonic flow through the bleed passage and avoids divergence in the early iterations before the bleed channel flow establishes itself.

5.4 Total Simulation Time

The physical end time was set to $t_{\text{end}} = 1.5\text{ms}$. At the Mach5 freestream velocity of 800 m s^{-1} over the domain length of 155 mm, one flow-through time is approximately 0.19 ms, meaning the simulation covers roughly 7.7 flow-through times, which is sufficient for the shock system and separation regions to reach a statistically steady state. The solution was written every 0.1 ms producing 15 snapshots for post-processing. All simulations were performed using OpenFOAM v2212.

5.5 Mesh Independence

A mesh independence study was conducted using four successively increasing grid levels, starting from 41,900, 99,000, 1,46,820, and 2,19,000 cells evaluated against the normalized wall pressure distribution P/P_∞ along the full inlet-isolator lower wall section, as shown in Figure 7. The coarsest mesh of 41,900 cells exhibits visible oscillations across the first ramp region and fails to capture the correct shock structure in the isolator, indicating insufficient resolution for the shock wave-boundary layer interactions present in this flow. Refining to 99,000 cells suppresses these oscillations and brings the overall pressure profile into closer agreement with the finer levels, though an offset remains visible in the isolator region, particularly near the peak pressure location. At 1,46,820 cells, the profile converges closely with that of the finest 2,19,000 cell mesh, with the two curves becoming visually indistinguishable throughout the entire domain, including the high-gradient isolator region where shock impingement, separation and reattachment features are most sensitive to grid density. Based on this convergence behavior, the 1,46,820 cell mesh was selected for all subsequent simulations as it delivers a grid-independent solution without incurring the additional computational expense of the finest level.

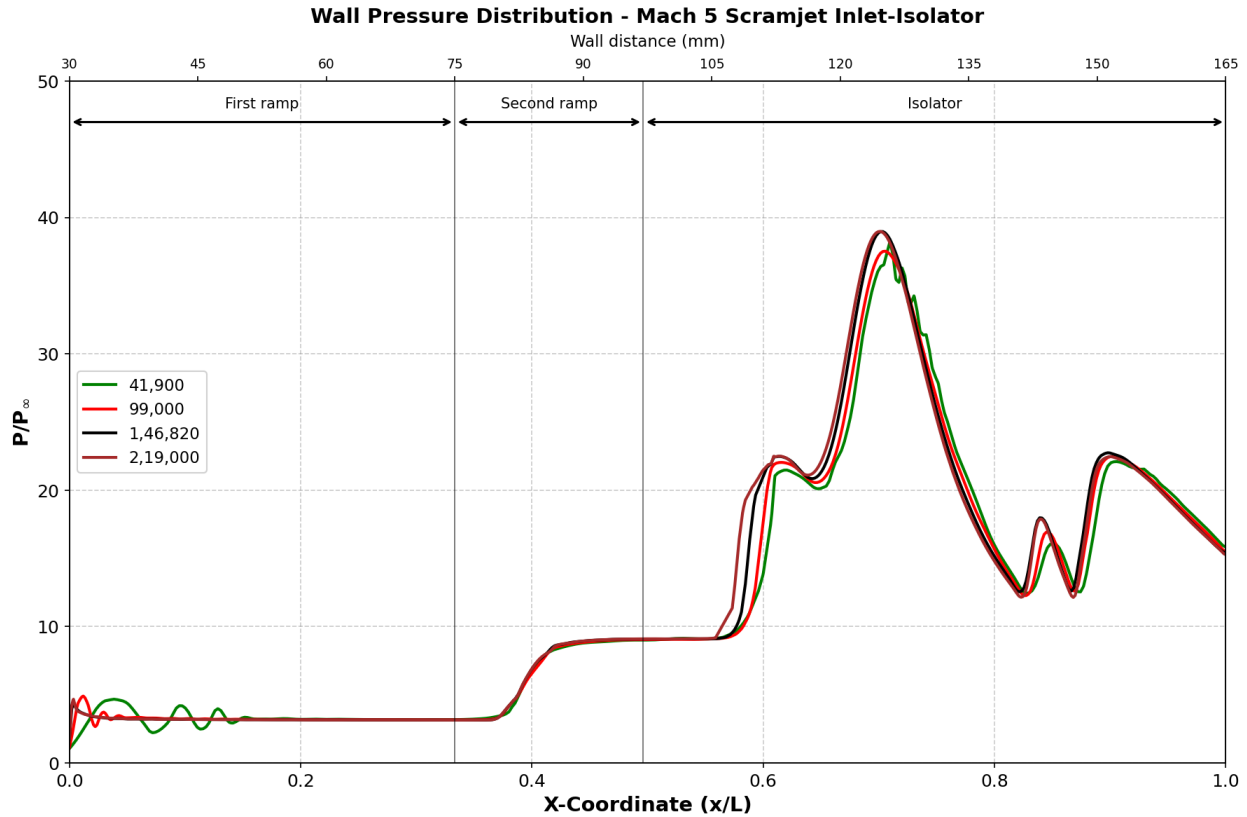


Figure 7: Mesh independence

6 Results and Discussion

6.1 Mach 5

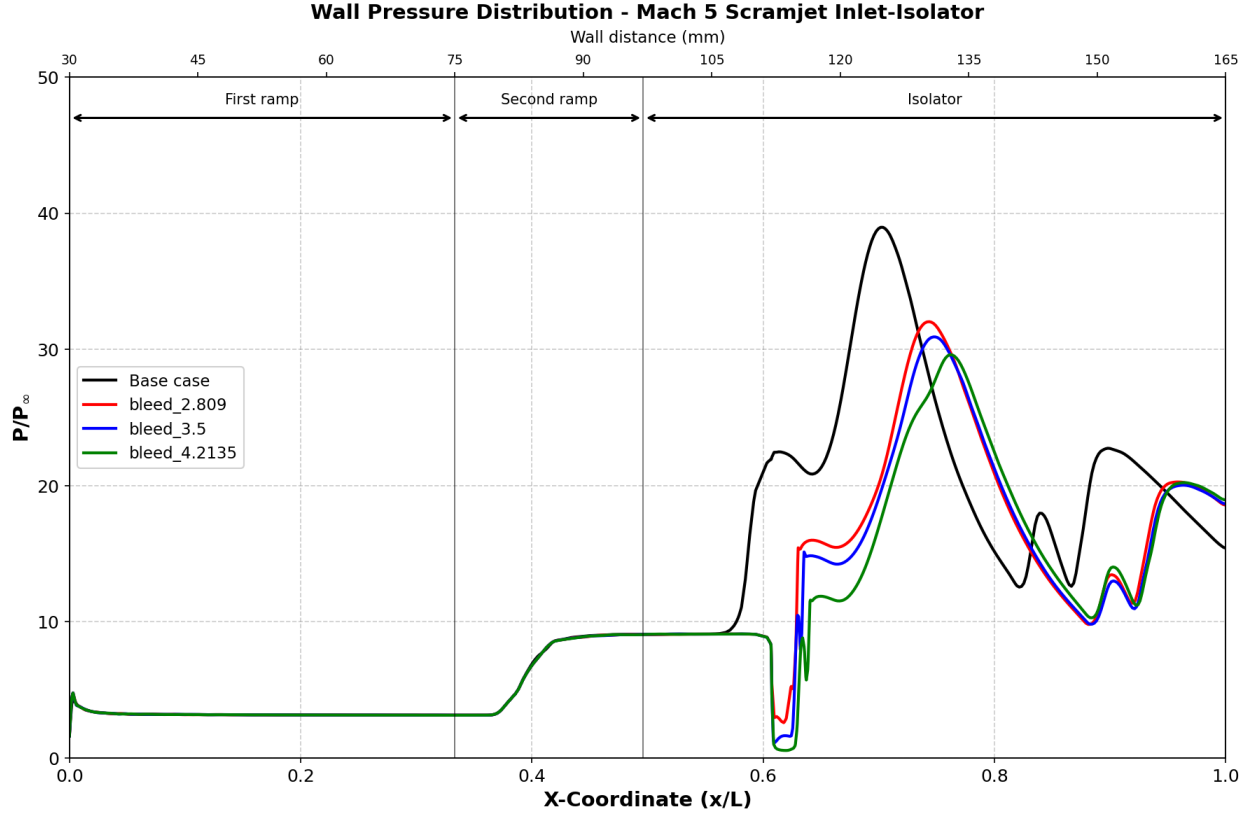


Figure 8: Wall Pressure distribution of Mach 5 base case with different bleed slots 2.809mm, 3.5mm and 4.2135mm

Figure 8 shows the normalized wall pressure distribution along the lower wall of the inlet-isolator. It shows that there is a dominant effect of bleed on the shock-wave/boundary layer interaction structure within the isolator. In the baseline case (Without bleed case), the pressure peaks sharply at $x/L=0.702$ with $P/P_\infty \approx 38.97$, coinciding with the impingement of the reflected cowl shock onto the lower isolator wall. The oscillations downstream of this peak are signatures of recirculating separation bubbles documented by (Idris et al., 2014), where the boundary layer repeatedly separates and reattaches under the adverse pressure gradient due to successive shock reflections.

With a 2.809mm bleed slot, the peak drops to 32.04 and shifts downstream to $x/L=0.743$, indicating that the bleeding has removed sufficient low-momentum fluid to prevent the boundary layer from separating as aggressively at the original impingement location which reorganizes the shock structure further in the isolator. The 3.5 mm and 4.2135 mm slots reduce the peak further to 30.92 at $x/L=0.747$ and 29.61 at $x/L=0.762$ respectively. The progressive downstream shifting of the peak pressure location with the increasing bleed width reflects a systematic weakening of the separation-induced shock train, as the bleed continuously draws off the near wall low velocity fluid

before it accumulated enough adverse momentum to start strong separation.

The mass-flow weighted total pressure recovery profile at the isolator exit in Fig: 9 confirm the performance enhancement due to boundary layer bleed across the full exit height. The baseline case achieves a pressure recovery of $\pi=0.2652$, consistent with severe entropy generation due to multiple shock reflection and separation bubble identified in the wall pressure.

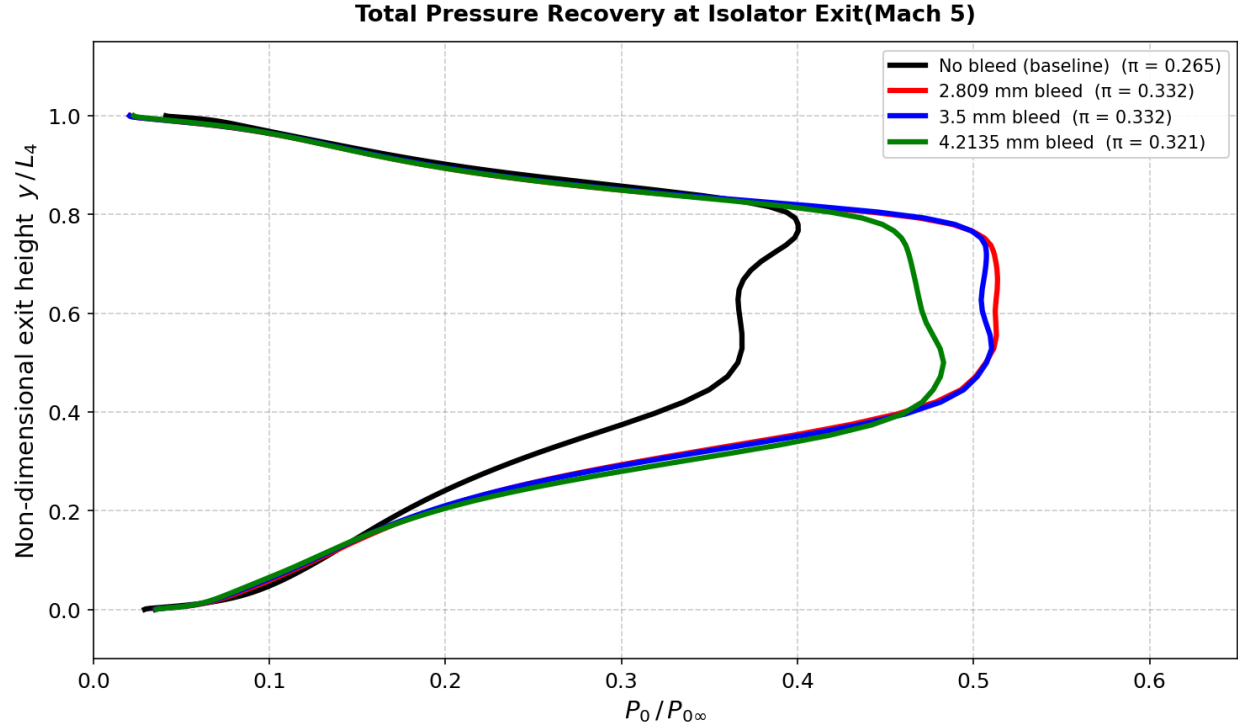


Figure 9: Total Pressure recovery at the isolator exit at different bleed width

All three bleed configuration improve this significantly. The 2.809mm bleed yields $\pi=0.3321$, a gain of 25.26% over baseline and the 3.5 mm slot produces a nearly identical $\pi=0.3318$ with a gain of 25.12% from the baseline, suggesting that the flow mechanism governing pressure recovery saturates between these two slot widths. The 4.2135 mm slot despite reducing the peak wall pressure the most delivers a low pressure recovery of $\pi=0.3206$ a 20.96% increase from baseline indicating that beyond a threshold bleed width the excessive removal of mass flow begins to deplete the core flow momentum and introduces additional losses at the bleed exit. The profile also shift, the bleed cases show a more uniform distribution across the exit height, whereas the baseline profile exhibits a profound deflection towards the wall-side consistent with the blockage effect of the large separation region. These result establish 2.809mm as the optimal bleed width for this geometry at Mach 5, balancing effective separation control against mass flow penalty.

Figure 10 shows the velocity contour for all cases of Mach 5. The base case of Fig 10a shows three distinct flow separation regions: Main separation at the isolator lower wall, cowl separation and the downstream separation. The cowl separation and downstream separation are completely depleted for all the bleed cases showing proper implementation of bleed.

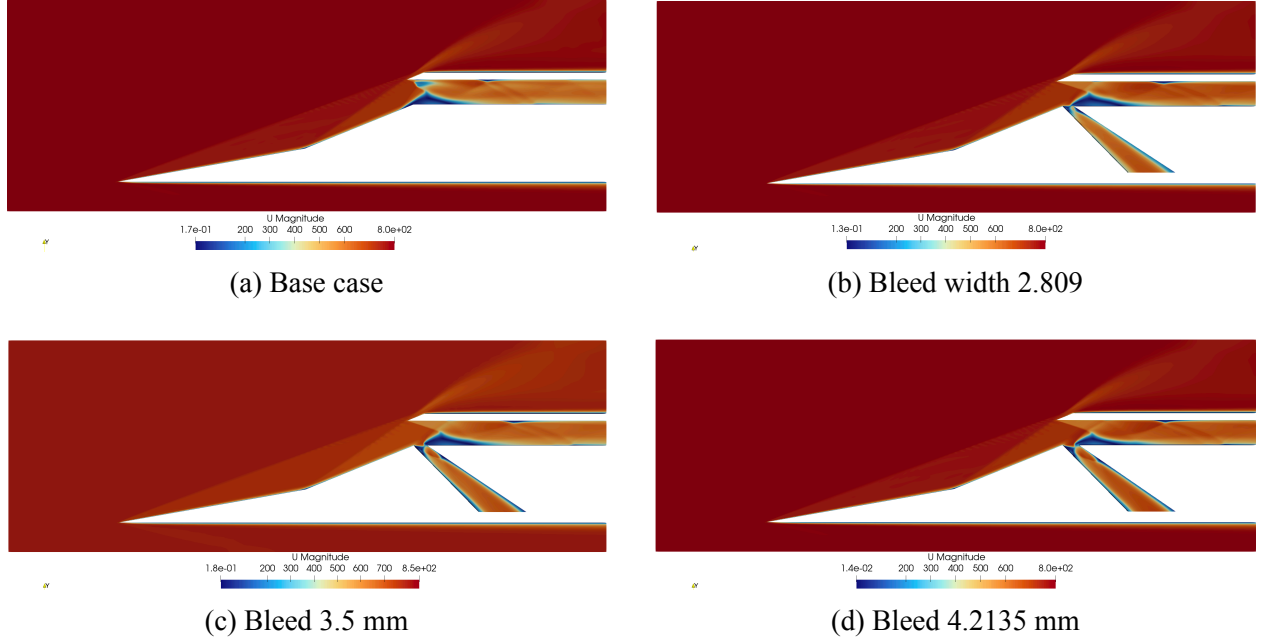


Figure 10: Velocity contour of Mach 5 cases.

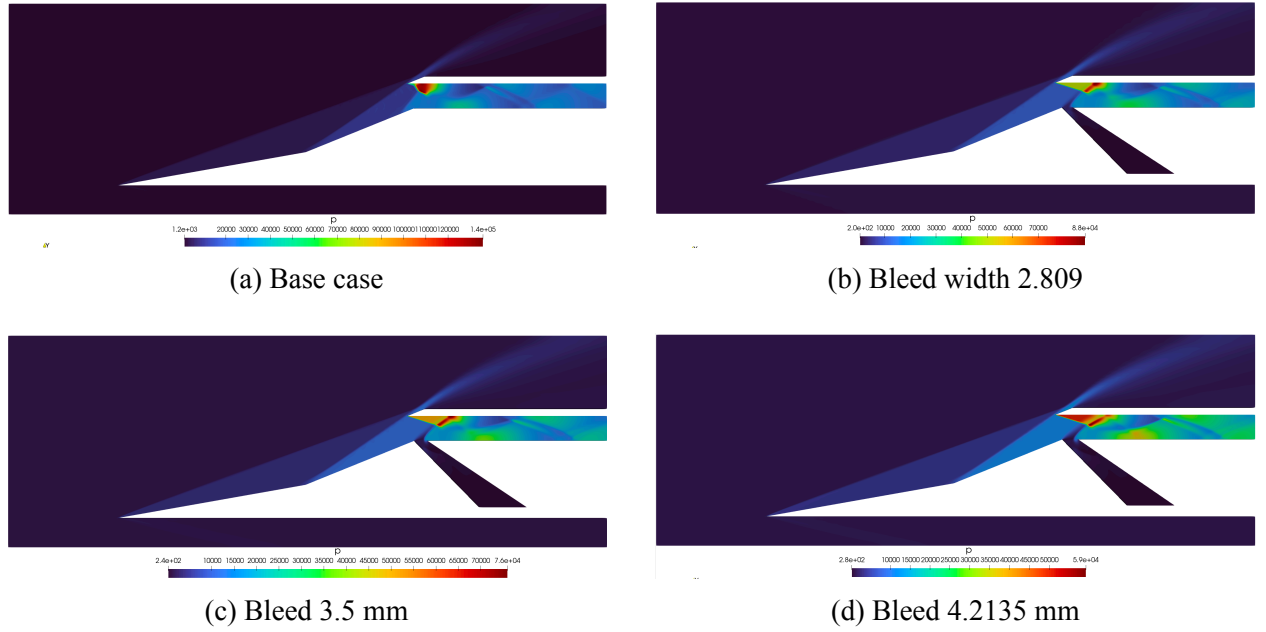


Figure 11: Pressure contour of Mach 5 cases.

Figure 11 shows the pressure contour of all Mach 5 cases. The base case 11a shows high pressure near the cowl due to the reflected shock wave from the cowl. A distinct shock train structure is visible inside the isolator. The bleed cases show that the high pressure area near cowl is shifted downstream with dissipation of pressure, a shock train is also visible in the bleed cases.

6.2 Mach 6

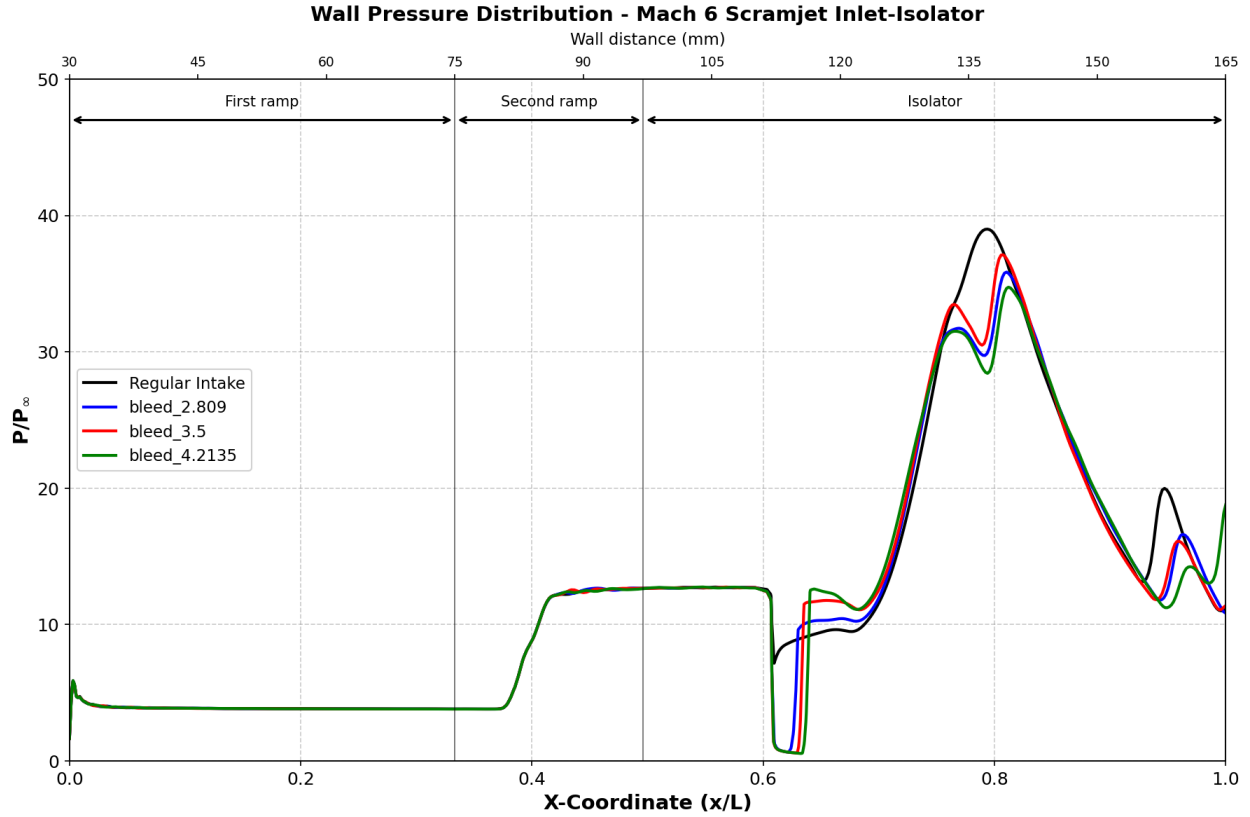


Figure 12: Wall Pressure distribution of Mach 6 base case with different bleed slots 2.809mm, 3.5mm and 4.2135mm.

At Mach 6 the geometry operates outside of its design, the shock-on-lip condition that was satisfied at Mach 5 is no longer met. The shallower shock angles due to high mach number causes the second ramp oblique shock to overshoot the cowl leading edge, changing the entire shock impingement geometry inside the isolator. As a result, the peak pressure location shifts and the amplitude of the downstream oscillations is reduced in comparison to the Mach 5 as the shock train has reorganized into a different configuration with different impingement location. All four curves (Baseline and three bleed slots) in Fig 13 are nearly coincident throughout the isolator, indicating that the bleed slot at the entrance is no longer intercepting the low-momentum fluid at the most damaging separation point mainly due to off design conditions.

The total pressure recovery confirms the marginal effect of bleed at this mach number. The baseline achieves $\pi=0.229$ and the best bleed configurations 2.890mm and 4.2135 mm reach only $\pi=0.233$ a gain of around 2%. The dominant loss mechanism at Mach 6 is due to increased entropy generation from stronger oblique shocks and the change in shock-on-shock interaction near the cowl.

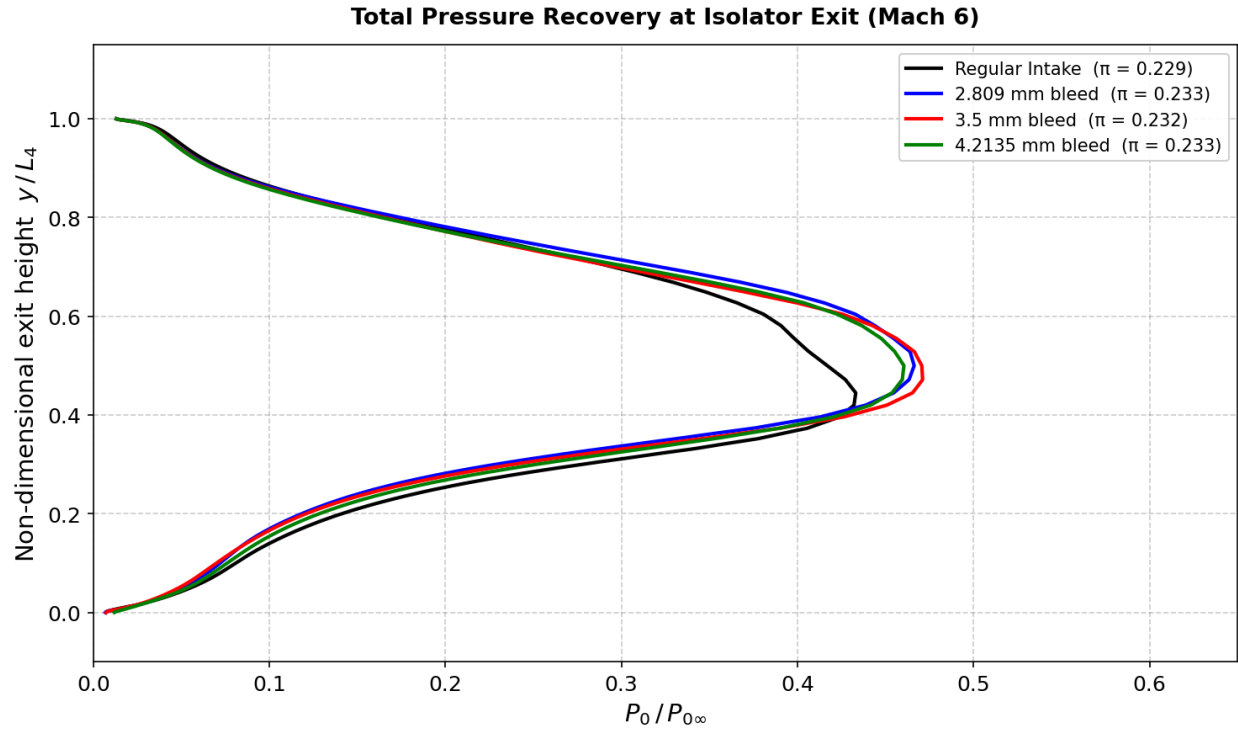


Figure 13: Total Pressure recovery at the isolator exit with different bleed configurations Mach 6

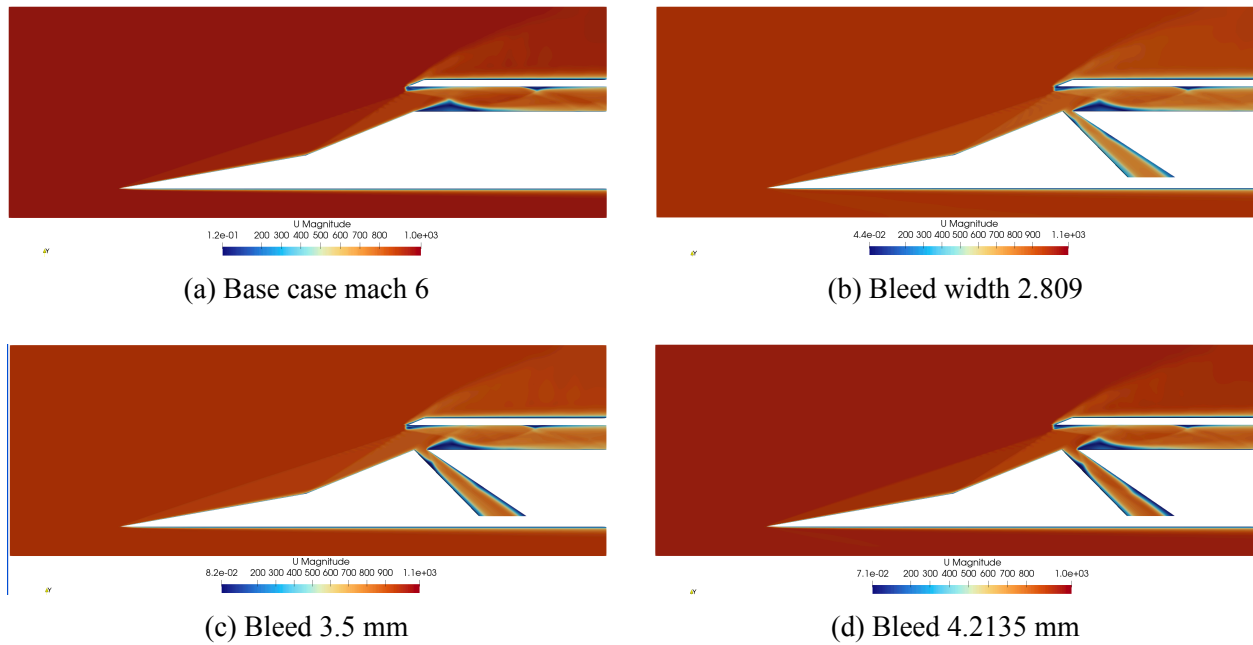


Figure 14: Velocity contour of Mach 6 cases.

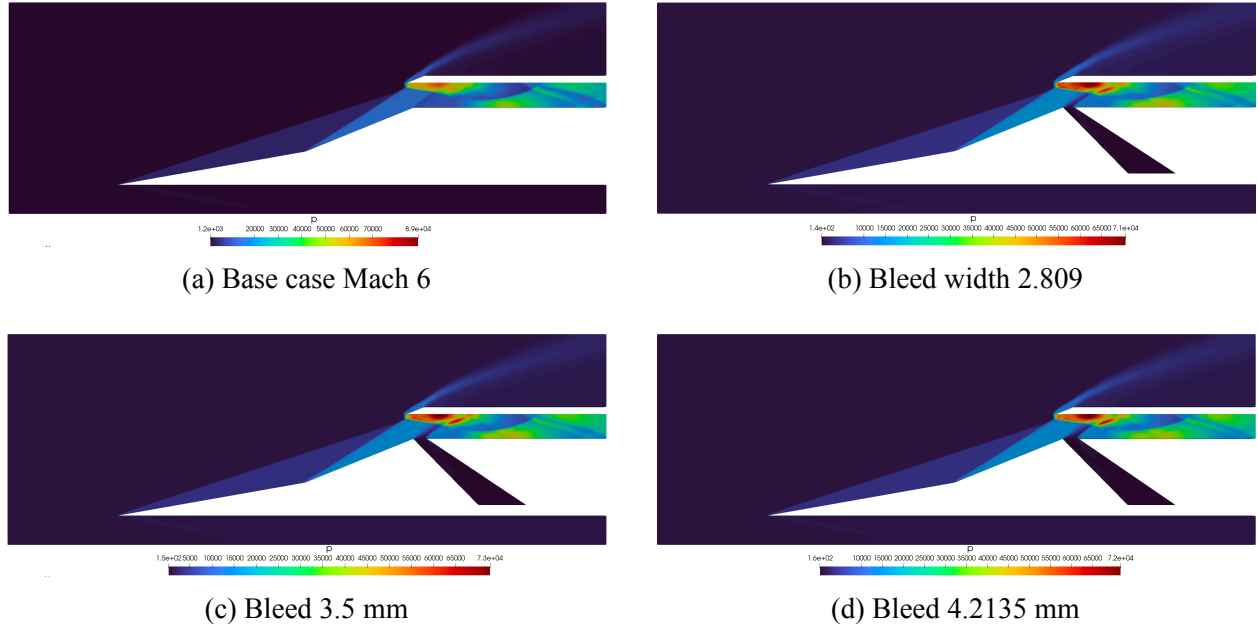


Figure 15: Pressure contour of Mach 6 cases.

The velocity contours in Fig 14 show a noticeably different separation topology as compared to Mach 5. The base case no longer shows three clearly distinct separation bubbles, instead a single large low-velocity region dominates the lower isolator wall, reflecting the altered impingement geometry. The cowl separation visible at Mach 5 is replaced by a different interaction pattern where the shock from the second ramp impinges further downstream along the isolator rather than at the cowl lip. The bleed cases show only a marginal reduction in this separation region, consistent with the negligible total pressure recovery improvement. The pressure contours in Fig 15 shows: the high-pressure kernel near the cowl is more diffuse and located further downstream than at Mach 5, and the shock train inside the isolator appears less organized. The bleed cases produce a small redistribution of the pressure near the slot exit but the global pressure field is essentially unchanged.

6.3 Mach 7

At Mach 7 the shock misalignment is more severe and the peak wall pressure rises due to the stronger normal component of the impinging shock wave as seen in Fig 16. This is physically expected as at this mach number the separation region is primarily driven by the intense adverse pressure gradient of the stronger shock and the momentum deficit in the near wall region has grown beyond what a passive fixed geometry can remedy by mass removal.

The total pressure recovery at Mach 7 in Fig 17 is reduced to $\pi=0.165$ for the baseline, and the improvements from bleed slots are negligible, the 2.809 mm slot reaches $\pi=0.169$ while the 4.2135 mm slot matches the baseline exactly at $\pi=0.165$. This effectively means the largest bleed configuration provides no benefit at all, because the mass it extracts only helps the downstream flow without suppressing the separation. The exit profiles of all four cases are nearly same, with only a slight divergence near the channel mid-height for the 2.809 mm case.

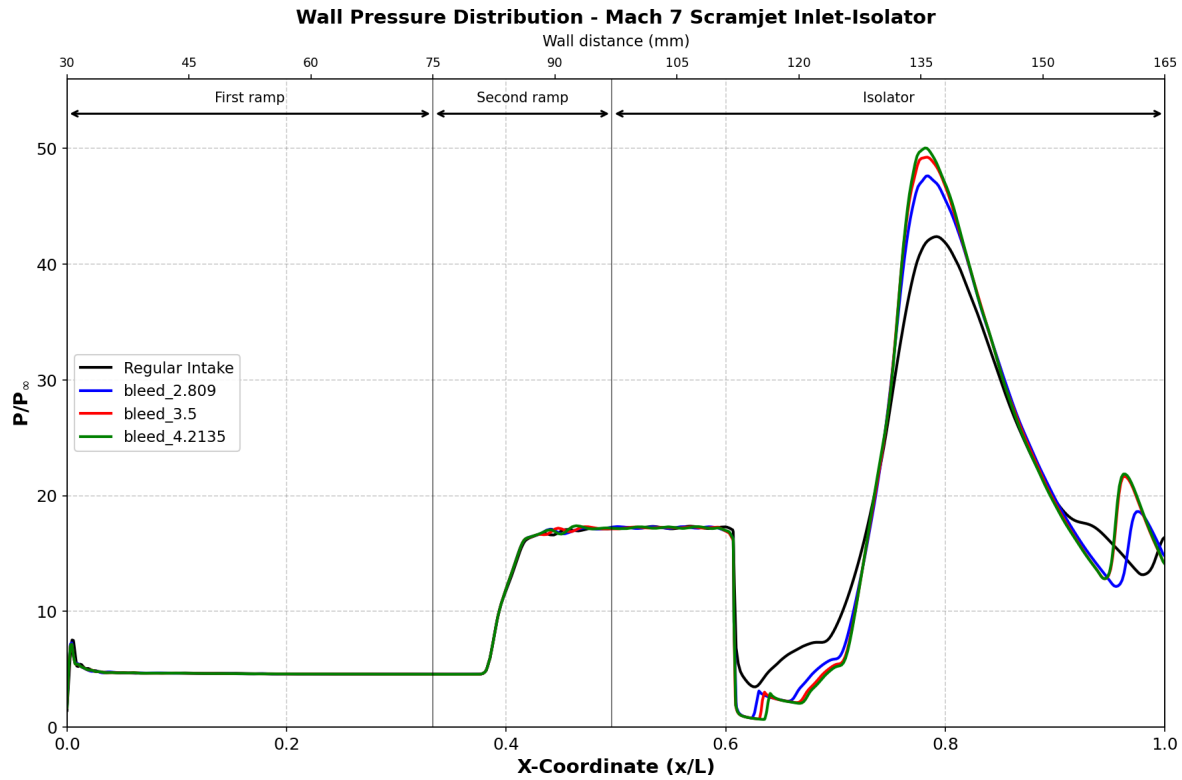


Figure 16: Wall Pressure distribution of Mach 7 base case with different bleed slots 2.809mm, 3.5mm and 4.2135mm.

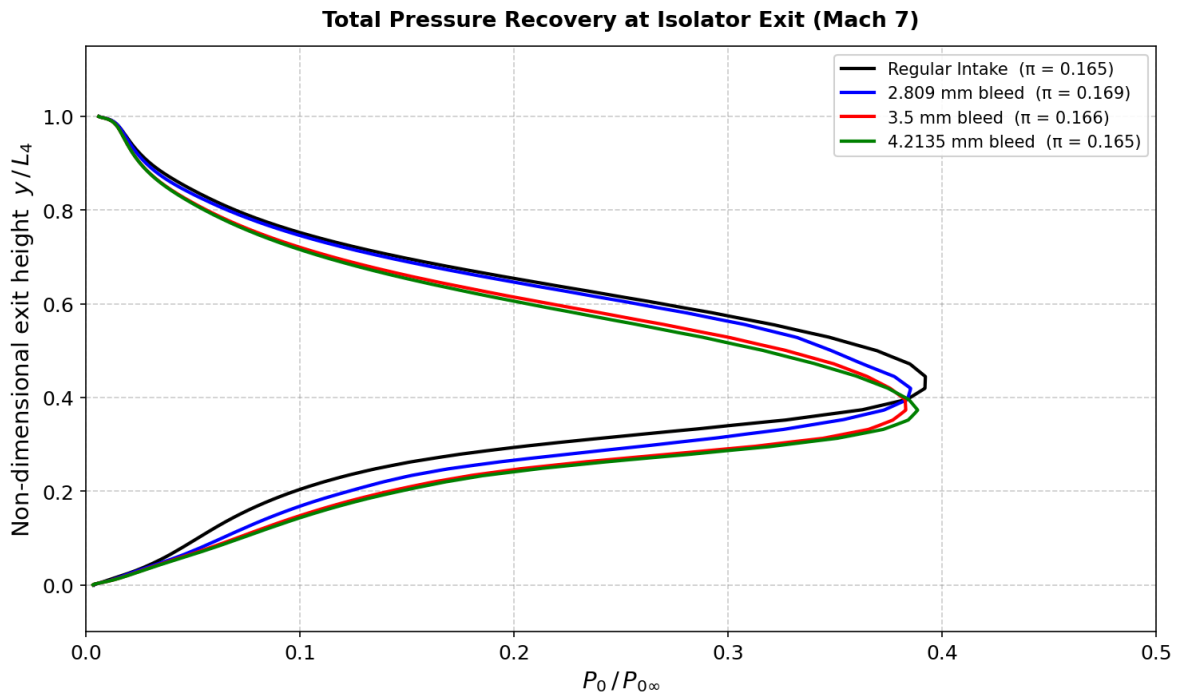


Figure 17: Total Pressure recovery at the isolator exit with different bleed configurations Mach 7

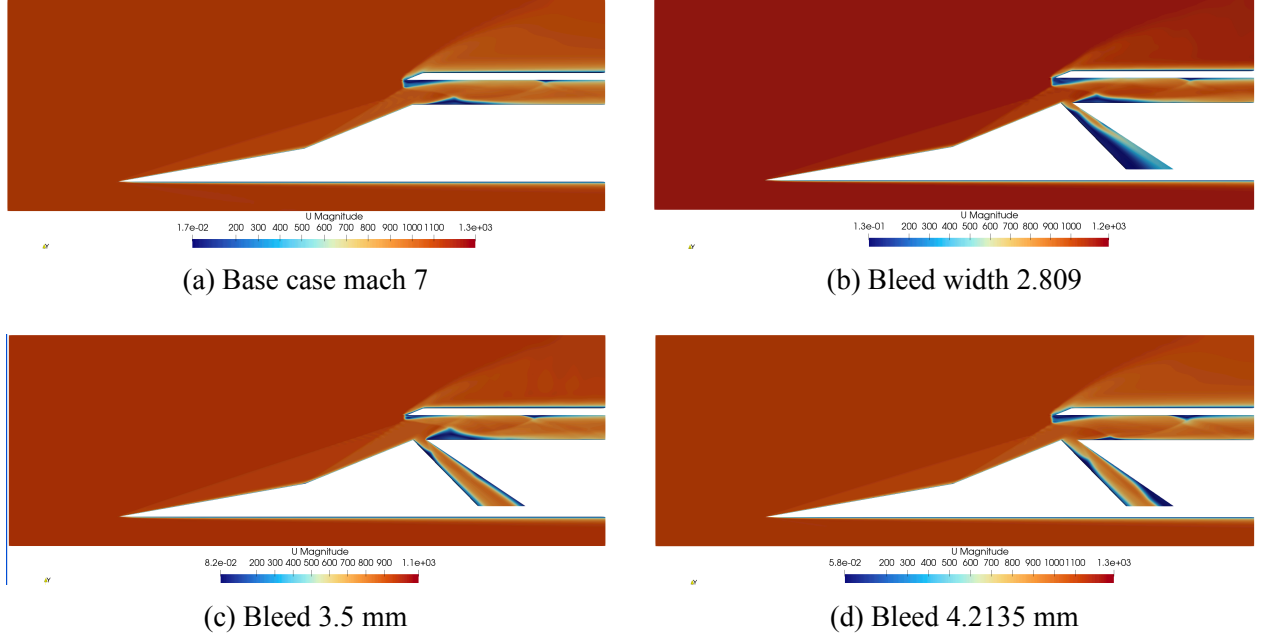


Figure 18: Velocity contour of Mach 7 cases.

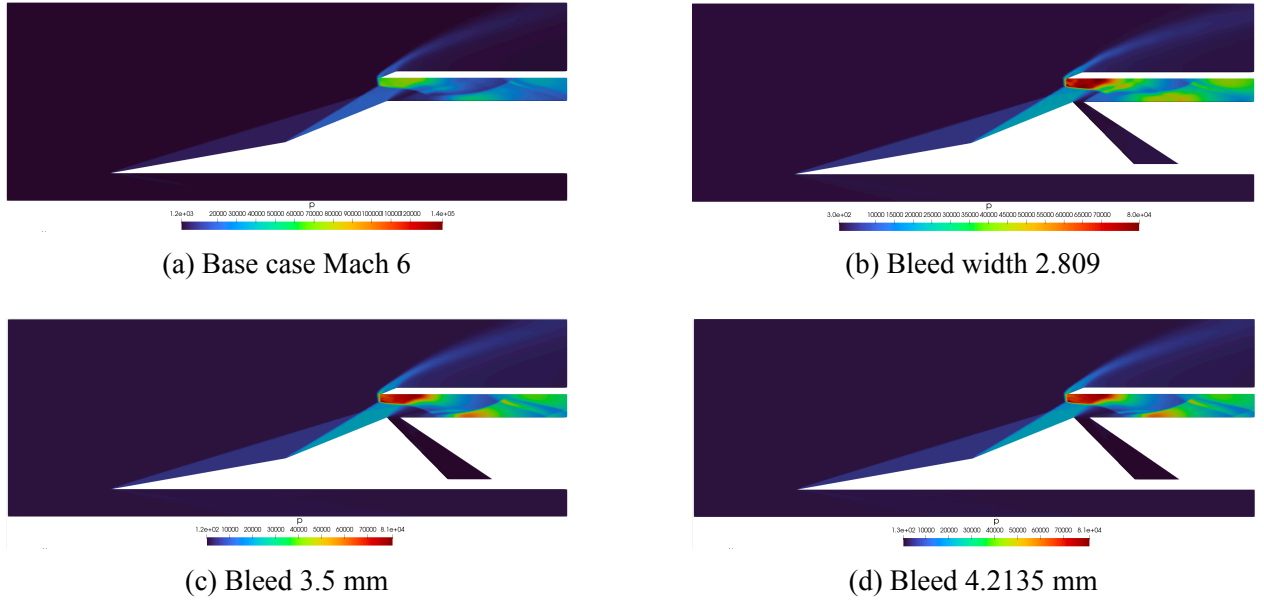


Figure 19: Pressure contour of Mach 7 cases.

The velocity contours at Mach 7 show a enlarged low-velocity separation zone in the base case, now occupying a significant fraction of the lower isolator height and extending further downstream than at any lower Mach number. The separation like low velocity region is seen dominated near cowl which is formed entirely due to stronger normal shock wave forming at the cowl tip as seen in Fig 18a. The pressure contours in Fig 19 show that the oblique shock from the second ramp and the subsequent reflections produce a pressure field with a more extended high-pressure tongue

along the upper wall, characteristic of the shock train shifting toward the cowl wall under stronger interaction conditions. The bleed produces no visible change in the pressure contour structure, and the shock reflection pattern inside the isolator is indistinguishable between cases.

6.4 Comparative Performance

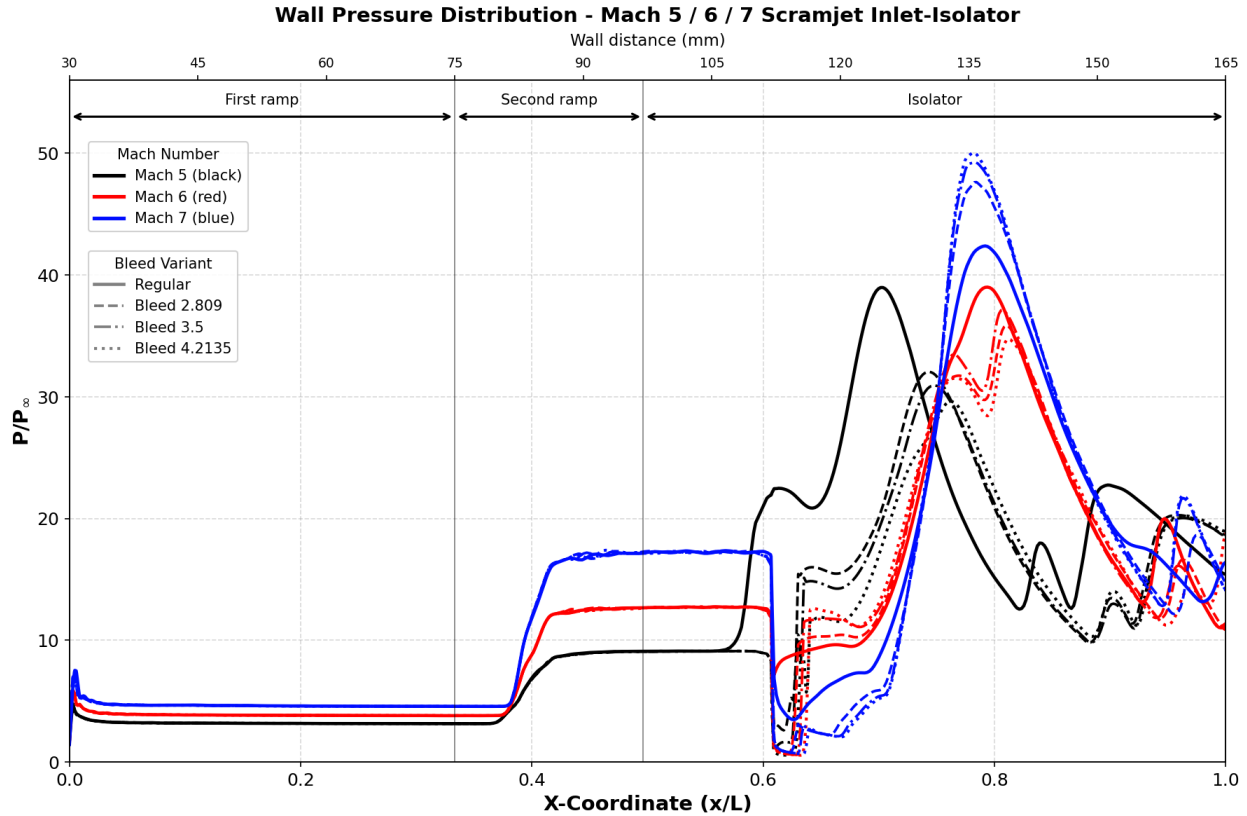


Figure 20: Combined pressure ratio for mach 5, 6 & 7 with base case and their bleed case

The combined wall pressure plot Fig 20 across all three mach number reveals clear two trends: a) the peak pressure rises with Mach number caused due to increasing strength of the impinging oblique shock wave, b) the difference between baseline and bleed curves reduces from Mach 5 to Mach 7. This makes it clear that the geometry and the bleed section was sized and positioned for the Mach condition and loses authority as the shock system changes with mach number.

The combined recovery plot Fig 21 shows the overall performance across the flight mach range, Total pressure recovery falls with Mach number regardless of bleed due to stronger shock waves forming at higher speed. At Mach 5 the bleed cases showed the best result with almost 25% increase in pressure, however for Mach 6 and 7 this increase is very marginal. While taking everything together, the plots confirm that the passive bleed technique is very effective at design conditions but at off design condition its benefits reduce.

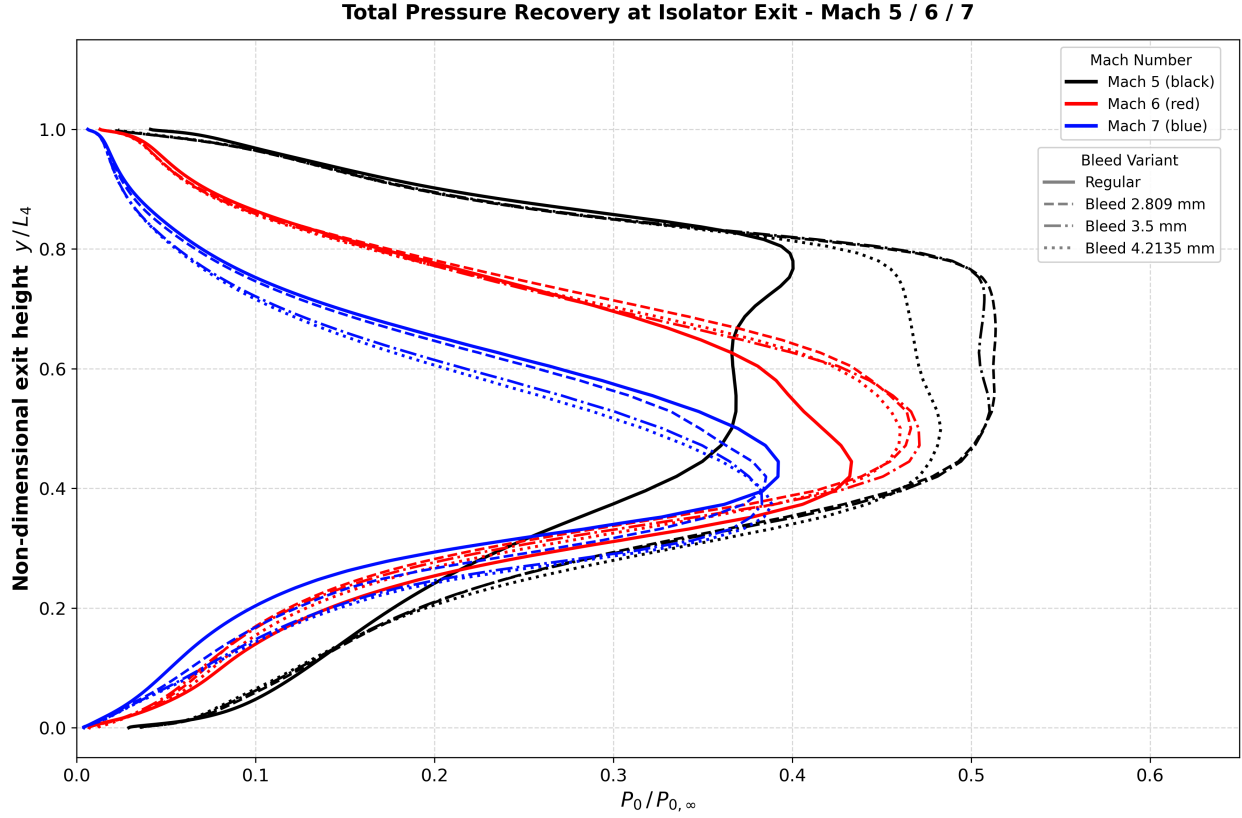


Figure 21: Combined Total Pressure recovery for Mach 5, 6 & 7 cases

7 Conclusion

This study thus demonstrates that an OpenFOAM based framework using rhoCentralFoam with SST $k - \omega$ turbulence model can reproduce a complex shock-wave/boundary layer interaction physics of double ramp scramjet inlet-isolator, enabling us to use it as a predictive tool for intake flow research. At design mach number (Mach 5) passive boundary layer bleed proves very effective with bleed slot 2.809mm and 3.5 mm being optimum configuration increasing the total pressure recovery by more than 25% by removing near wall low momentum fluid before it forms separation bubble. However for off design condition (Higher mach number), the total pressure recovery fails to provide good results mainly due to not fulfilling shock-on-lip condition, producing a different shock pattern inside the isolator.

8 Future Scopes

- **Three dimensional Simulations:** This present work is restricted to a 2d planar geometry. Extending the domain to three dimensions would capture side wise boundary layer, corner separation and spanwise non-uniformity.
- **SOL geometry for variable speed range:** The present geometry was designed specifically

designed for Mach 5, where the oblique shock waves impinge directly on the cowl, thus shock-on-lip(SOL) condition is fulfilled, however as seen in Mach 6 and 7 the shock waves doesn't impinge on the cowl changing the shock structure inside isolator. Thus, redesigning geometry to meet SOL at multiple mach numbers through variable ramp angles or multi-point design approach.

- **Multi-objective optimization of bleed slot:** Only slot width was varied in this work keeping position and shape same. Therefore, a study with change in these parameters can be done.

References

- Bajaj, D. K., Kansara, S. T., Nath, N. K., Vashishtha, A., & Sahoo, D. (2025). Enhancement of scramjet inlet efficiency by geometrical modifications. *Advances in Aerodynamics*, 7(6). <https://doi.org/10.1186/s42774-025-00206-7>
- Idris, A. C., Saad, M. R., Zare-Behtash, H., & Kontis, K. (2014). Luminescent measurement systems for the investigation of a scramjet inlet-isolator. *Sensors*, 14(4), 6606–6632. <https://doi.org/10.3390/s140406606>
- Kantrowitz, A., & Donaldson, C. d. (1945). *Preliminary investigation of supersonic diffusers* (tech. rep. No. NACA-WR-L-713). National Advisory Committee for Aeronautics. Hampton, VA, USA.
- Menter, F. R. (1994). Two-equation eddy-viscosity turbulence models for engineering applications. *AIAA Journal*, 32(8), 1598–1605.
- Sandeep, J., & Gupta, A. V. S. S. K. S. (2024). Assessment of the hypersonic intake isolator and performance evaluation at various flight conditions. *Aerospace Systems*. <https://doi.org/10.1007/s42401-024-00316-y>
- Sandeep, J., & Gupta, A. V. S. S. K. S. (2023). Grid adaptive technique for simulation of scramjet intake-isolator at hypersonic speeds. *Journal of Advanced Research in Fluid Mechanics and Thermal Sciences*, 101(1), 73–89. <https://doi.org/10.37934/arfmts.101.1.7389>